[O III] EMISSION AND GAS KINEMATICS IN A LYMAN-ALPHA BLOB AT $z \sim 3.1$

Emily M. McLinden[1], Sangeeta Malhotra[2], James E. Rhoads[2], Pascale Hibon[3],
Anne-Marie Weijmans[4], and Vithal Tilvi[5]

[1] McDonald Observatory, University of Texas at Austin, Austin, TX 78712, USA
[2] School of Earth and Space Exploration, Arizona State University, Tempe, AZ 85287, USA
[3] Gemini Observatory, La Serena, Chile
[4] Dunlap Institute for Astronomy & Astrophysics, University of Toronto, 50 St. George Street, Toronto, ON M5S 3H4, Canada
[5] George P. and Cynthia Woods Mitchell Institute for Fundamental Physics and Astronomy, and Department of Physics and Astronomy,
Texas A&M University, College Station, TX 77843, USA

ABSTRACT

We present spectroscopic measurements of the [O III] emission line from two subregions of strong Lyα emission in a radio-quiet Lyman-alpha blob (LAB). The blob under study is LAB1 at $z \sim 3.1$, and the [O III] detections are from the two Lyman break galaxies (LBGs) embedded in the blob halo. The [O III] measurements were made with LUCIFER on the 8.4 m Large Binocular Telescope and NIRSPEC on 10 m Keck Telescope. Comparing the redshift of the [O III] measurements to Lyα redshifts from SAURON allows us to take a step toward understanding the kinematics of the gas in the blob. Using both LUCIFER and NIRSPEC we find velocity offsets between the [O III] and Lyα redshifts that are modestly negative or consistent with 0 km s^{-1} in both subregions studied (ranging from -72 ± 42–$+6 \pm 33$ km s^{-1}). A negative offset means Lyα is blueshifted with respect to [O III] a positive offset then implies Lyα is redshifted with respect to [O III]. These results may imply that outflows are not primarily responsible for Lyman alpha escape in this LAB, since outflows are generally expected to produce a positive velocity offset. In addition, we present an [O III] line flux upper limit on a third region of LAB1, a region that is unassociated with any underlying galaxy. We find that the [O III] upper limit from the galaxy-unassociated region of the blob is at least 1.4–2.5 times fainter than the [O III] flux from one of the LBG-associated regions and has an [O III] to Lyα ratio measured at least 1.9–3.4 times smaller than the same ratio measured from one of the LBGs.

Key words: galaxies: high-redshift – galaxies: kinematics and dynamics – intergalactic medium

Online-only material: color figures

1. INTRODUCTION

Lyman-alpha (Lyα) first became a useful tool for observing high-z sources with the discovery of large samples of Lyα emitting galaxies (LAEs; Cowie & Hu 1998; Hu et al. 1998; Rhoads et al. 2000). The same narrowband imaging techniques that uncovered LAEs began uncovering a different set of objects that were also very bright in Lyα. These rarer, more extended, and more luminous objects are what we now call Lyα blobs (LABs; e.g., Steidel et al. 2000; Francis et al. 2001; Matsuda et al. 2004; Dey et al. 2005; Nilsson et al. 2006; Prescott et al. 2012). LABs are extremely large ($\sim$30–200 kpc) radio-quiet Lyα nebulae in the high redshift universe. LABs are highly luminous ($L_{\mathrm{Ly}\alpha} \sim 10^{43}$–$10^{44}$ erg s^{-1}), and yet despite rigorous study in the last decade, the mechanism(s) that power this immense Lyα flux is not fully understood. This paper will focus on investigating the kinematics of and mechanisms powering such objects by investigating LAB1, a $z \sim 3.1$ LAB first discovered by Steidel et al. (2000).

There are currently three widely discussed scenarios to explain both the large spatial extent and powerful Lyα flux of these blobs. The first of these is that the gas in LABs is heated by photoionization from massive stars and/or active galactic nuclei (AGNs; Geach et al. 2009). A second scenario proposes that gas in LABs is heated by cooling flows/cold accretion (Haiman et al. 2000; Dijkstra & Loeb 2009). Finally, some authors have proposed that LABs originate from overlapping supernova remnants from massive stars after a powerful starburst (Taniguchi & Shioya 2000; Ohyama et al. 2003) producing superwinds.

Adding to the controversy, observations in recent years from different authors have led to different conclusions about which of these scenarios are responsible for said observations. Nilsson et al. (2006) have argued that their observations of a $z \sim 3.16$ LAB were best matched by cooling flows onto a dark matter halo. This can be compared to the observations of Hayes et al. (2011), who found evidence of polarized Lyα radiation in LAB1. The Hayes et al. (2011) results suggest that Lyα photons are scattered at large radii from their production sites and indicate a homogeneous scattering medium (at least on the scales probed by their resolution elements). However, the imaging polarization analysis alone cannot set constraints on the gas kinematics, but the authors contend their discovery disfavors filamentary inflow models. But a similar study by Prescott et al. (2011) found no evidence of polarization in a LAB at $z \sim 2.656$ and these authors argue their results are inconsistent with spherical outflows and Lyα scattering from nearby AGNs. Yet another conclusion is reached by Yang et al. (2011) whose observations of Lyα and Hα emission in two $z \sim 2.3$ LABs rule out simple infall models and models that rely on large outflows. This diversity of conclusions may mean that there are diverse mechanisms powering different blobs (or multiple mechanisms at play in single blobs) or it may mean that truly conclusive observations have not yet been presented.

To try to provide new data to differentiate among the possible LAB sources we focus on LAB1 (Steidel et al. 2000). LAB1 resides in SSA22, a protocluster region at $z \sim 3.1$ (Steidel et al. 1998). LAB1 extends $\sim$100 kpc (Weijmans et al. 2010) and has a Lyα luminosity of 1.1×10^{44} erg s^{-1} (Matsuda et al. 2004). This makes LAB1 one of the brightest and most spatially extended

LABs yet observed (Steidel et al. 2000; Matsuda et al. 2004). LAB1 is comprised of five separate regions of Lyα emission known as C11, C15, R1, R2, and R3 (see Figure 1 of Weijmans et al. 2010). C11 and C15 are both Lyman break galaxies (LBGs) identified by Steidel et al. (2000). R3 has been identified as an extremely red galaxy (Geach et al. 2007) and may or may not be associated with a bright submillimeter source and nearby radio source (Chapman et al. 2001, 2004; but see also Kohno et al. 2008; Yang et al. 2012). R1 and R2 are not identified with galaxies (Weijmans et al. 2010). Geach et al. (2009) also demonstrated that AGN activity is not significant in LAB1 as LAB1 is not detected in a 400 ks *Chandra* exposure. We note that Matsuda et al. (2004) identified C15 as a separate LAB, but in this paper we refer to all five subregions as components of LAB1, following the nomenclature of Steidel et al. (2000) and Weijmans et al. (2010).

In this paper we present new spectroscopic [O III] observations of LAB1. We focus on the two Lyα subregions C15 and C11, the two parts of the larger LAB1 structure in which we detected [O III]. The use of [O III] to study the kinematics of LAB1 is powerful because [O III] is not subject to resonant scattering as Lyα is. Comparing [O III] to Lyα emission allows us to characterize any systemic offsets between Lyα and [O III], and thereby detect the presence of outflows or inflows. We first demonstrated the efficacy of this method in a sample of LAEs in McLinden et al. (2011).

Our new [O III] data presented here are compared to Lyα data originally presented in Weijmans et al. (2010). Weijmans et al. (2010) measured Lyα from each of the five subregions in LAB1 with the integral field spectrograph SAURON (Bacon et al. 2001) over 23.5 hr (including 9 hr of SAURON data originally obtained by Bower et al. 2004). We obtained the reduced datacube produced from these observations from Weijmans. This allows us to extract Lyα profiles at locations corresponding to our NIR [O III] observations for careful comparison of [O III] and Lyα redshifts. Henceforth we refer to Weijmans et al. (2010) as W10.

In Sections 2 and 3 we present our [O III] detections from two near-infrared (NIR) spectrographs (NIRSPEC and LUCIFER). In Section 5 we look for any velocity offsets between our measured [O III] redshifts and those of Lyα to look for any evidence of inflows or outflows and in Section 6 we discuss the implications of our findings of velocity offsets (Δv) that are modestly negative or consistent with zero. We also compare our results to other authors and explore if there are currently any Lyα radiative transfer models that can match our results. Where relevant, we adopt the standard cosmological parameters $H_0 = 70 \, \mathrm{km \, s^{-1} \, Mpc^{-1}}, \Omega_m = 0.3$, and $\Omega_\Lambda = 0.7$ (Spergel et al. 2007). We use the following vacuum wavelengths, 1215.67 Å for Lyα, 3727.092/3729.875 Å for [O II], 4862.683 Å for Hβ, and 4960.295/5008.240 for [O III] from the Atomic Line List v2.04.[6]

2. NIRSPEC DATA AND REDUCTION

We initially detected [O III] emission from LAB1 using the near-infrared spectrograph NIRSPEC (McLean et al. 1998) on the 10 m Keck II telescope on 2010 August 6 (UT). We used the low-resolution mode of NIRSPEC, with the $42'' \times 0\farcs76$ slit and the NIRSPEC-6 filter which covers 1.558–2.315 μm. The spectral resolution of NIRSPEC in this setup is ~290 km s^{-1}. This filter encompasses the redshifted ($z \sim 3.1$) [O III] doublet and covers redshifted Hβ as well, though we did not see this line.

We completed three 500 s integrations for a total exposure of 25 minutes. The longslit was oriented so that LAB1 regions C15 and C11 (Steidel et al. 2000) both lie directly on the slit. Region R2 also has some peripheral coverage, though not directly through the location of its peak Lyα emission. Due to the short length of slit we were unable to place an additional continuum-bright object on the slit, so LAB1 was acquired via blind-acquisition from a nearby star.

[O III] detections from C15 and C11 are evident in single, raw 500 s exposures, when a second frame is subtracted from the frame of interest. We find these detections at their expected locations in the spatial direction along the slit, and find they also have the separation from one another that we expect for C11 and C15. In addition, the detections are in the wavelength range expected of each region's Lyα redshift. The dither pattern we used is also clearly visible in positive and negative detections when we perform this sort of quick-look subtraction, providing assurance that these detections are not transient cosmic rays, in a single exposure, see Figure 2. These facts combined give us confidence that the emission we detect is, in fact, from [O III] emission from C15 and C11. See the top panel of Figure 3 for these detections in a sky-subtracted 2D frame. The [O III] emission from C15 is strong and comes through as such in both our 2D and 1D reduction processes detailed below. The [O III] detections from C11 appear much fainter and are not as evident, though still marginally detected, throughout our 2D and 1D reduction processes.

Initial data reduction of each 500 s exposure was done using NIRSPEC_REDUCE, a set of IDL programs written by G. D. Becker specifically for reduction of NIRSPEC longslit data. We used these scripts for flat fielding and sky subtraction in each exposure. The sky subtraction process in NIRSPEC_REDUCE is based on the algorithm of D. Kelson (Kelson 2003) which provides excellent sky subtraction of even tilted skylines, such as those in NIRSPEC longslit data. The outcome of these reduction steps are three individual, 2D, flat-fielded, sky-subtracted exposures. We also reduced an argon lamp exposure and a standard star exposure in this same way.

We then fed these exposures into IRAF procedures in the WMKONSPEC package.[7] Each frame was rectified to a horizontal-vertical grid in *x–y* using the tasks XDISTCOR AND YDISTCOR, which remove *x* and *y* distortion in the images, respectively. Once the exposures were rectified, we used IMCOMBINE to median combine the frames into a single exposure. We specified offsets in the IMCOMBINE procedure to remove dithers along the slit that were performed during our observations. The result, what we call our reduced 2D spectrum, is shown in Figure 3. The locations of our [O III] detections in C11 and C15 are circled.

To extract 1D spectra we used the IRAF DOSLIT procedure. We first defined an aperture trace using a bright standard star observation which can be easily traced along the entire slit. We then transferred this aperture to the correct spatial locations in our science exposure to extract spectra of C15 and C11. We used this transferred aperture since neither region has continuum emission that we are able to trace for aperture creation. The spectra were wavelength calibrated using an argon lamp. The rms error from wavelength calibration was 0.67 and 0.45 Å for C15 and C11, respectively. We used the IRAF WMKONSPEC task SKYINTERP to remove remaining residuals from sky lines. The resulting 1D spectra from C15 and C11 are shown in Figure 3.
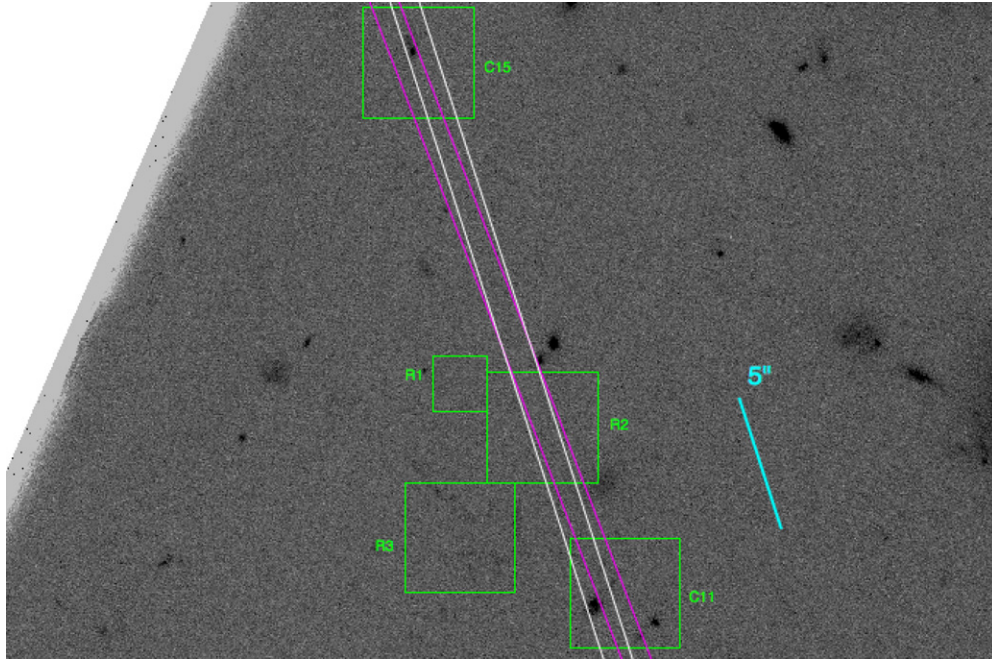

Figure 1. Orientation of longslit for NIRSPEC and LUCIFER observations. NIRSPEC slit is in white and LUCIFER slit is magenta. The boxes indicate the locations of subregions C11,C15, and R1-R3, from W10. Image from STIS-MIRVIS observations, retrieved from *Hubble Space Telescope* archives (Chapman et al. 2003).
(A color version of this figure is available in the online journal.)

Figure 2. Third NIRSPEC frame subtracted from second NIRSPEC frame, before *x*-axis and *y*-axis distortion correction, and sky subtraction. [O III] emission (5008.24 Å line) from C11 and C15 is more evident than in Figure 3. Emission from C15 is in cyan circles and emission from C11 is in green circles. Emission from second frame is black (positive) and emission from third frame is white (negative). Positive–negative dither pattern is clear, showing a detection in both frames displayed here.
(A color version of this figure is available in the online journal.)

We flux calibrate our NIRSPEC spectra using a magnitude 8.85 (*V* band) A1V star that was observed in the same setup as our science observations ($0\farcs76$ slit). We averaged an A0V and an A2V Pickles model spectrum to approximate an A1V spectrum. We then scaled down the A1V stellar spectrum (Pickles 1998) to match the magnitude of the observed star. We created a sensitivity function with units of erg cm^{-2} Å^{-1} counts^{-1} by dividing the model spectrum by the observed stellar spectrum and multiplying by the length of the observation. This sensitivity function is then multiplied by the extracted NIRSPEC spectra for C15 and C11, and then the result is divided by the integration time for each object to produce flux calibrated spectra in units of erg s^{-1} cm^{-2} Å^{-1}.

3. LUCIFER DATA AND REDUCTION

We subsequently made additional NIR observations of LAB1 using LUCIFER (LBT NIR Spectrograph Utility with Camera and Integral-Field Unit for Extragalactic Research) on the 8.4 m LBT (Seifert et al. 2003; Ageorges et al. 2010). We used the longslit mode of LUCIFER with a 1″ slit utilizing the H+K grating with 200 lines mm^{-1} and the N1.8 camera. LUCIFER has a spectral resolution of ∼318 km s^{-1} near 1.6 μm and

∼233 km s^{-1} near 2.2 μm. We combine three 300 s integrations for a total exposure of 15 minutes. We placed the longslit at a slightly different orientation than our NIRSPEC observations in hopes of capturing more emission from R2 and C15. For the LUCIFER setup, C15 and R2 lay directly on the slit, with part of C11 on the edge of the slit (see Figure 1). Given the length of the LUCIFER longslit, we were able to place a galaxy with continuum on the slit as well. This aids in aperture extraction during the reduction process.

We reduced the LUCIFER data in a very similar manner as the NIRSPEC data, but we used a modified version of the NIRSPEC_REDUCE package to accommodate the different detector size and orientation of the LUCIFER data. After the NIRSPEC_REDUCE procedures, the individual exposures were again median combined with IMCOMBINE and offsets from dithering along the slit were accounted for. Figure 4 shows the combined 2D spectrum after this step. For the 1D extraction, we created an aperture trace using the continuum source that shared the slit with our science targets, instead of the standard star as in our NIRSPEC procedure. Then we shifted the aperture to the correct spatial locations to extract 1D spectra for C15, C11, and R2. The spectra were again wavelength calibrated with an argon lamp exposure. Figure 4 shows the 1D extraction of C15 from our LUCIFER data, which was the only region from which we detected [O III] in our LUCIFER observations. We flux calibrate our LUCIFER spectra using a magnitude 6.16 (*V* band) A5V star that was observed in the same setup as our science observations (1″ slit). We used a Pickles A5V model spectrum and otherwise the calibration process is otherwise the same as described in Section 2.

4. Lyα DATA

We extracted Lyα profiles from the reduced SAURON datacube, data that were initially presented in W10. The SAURON data were registered to the *R*-band image that was used to align
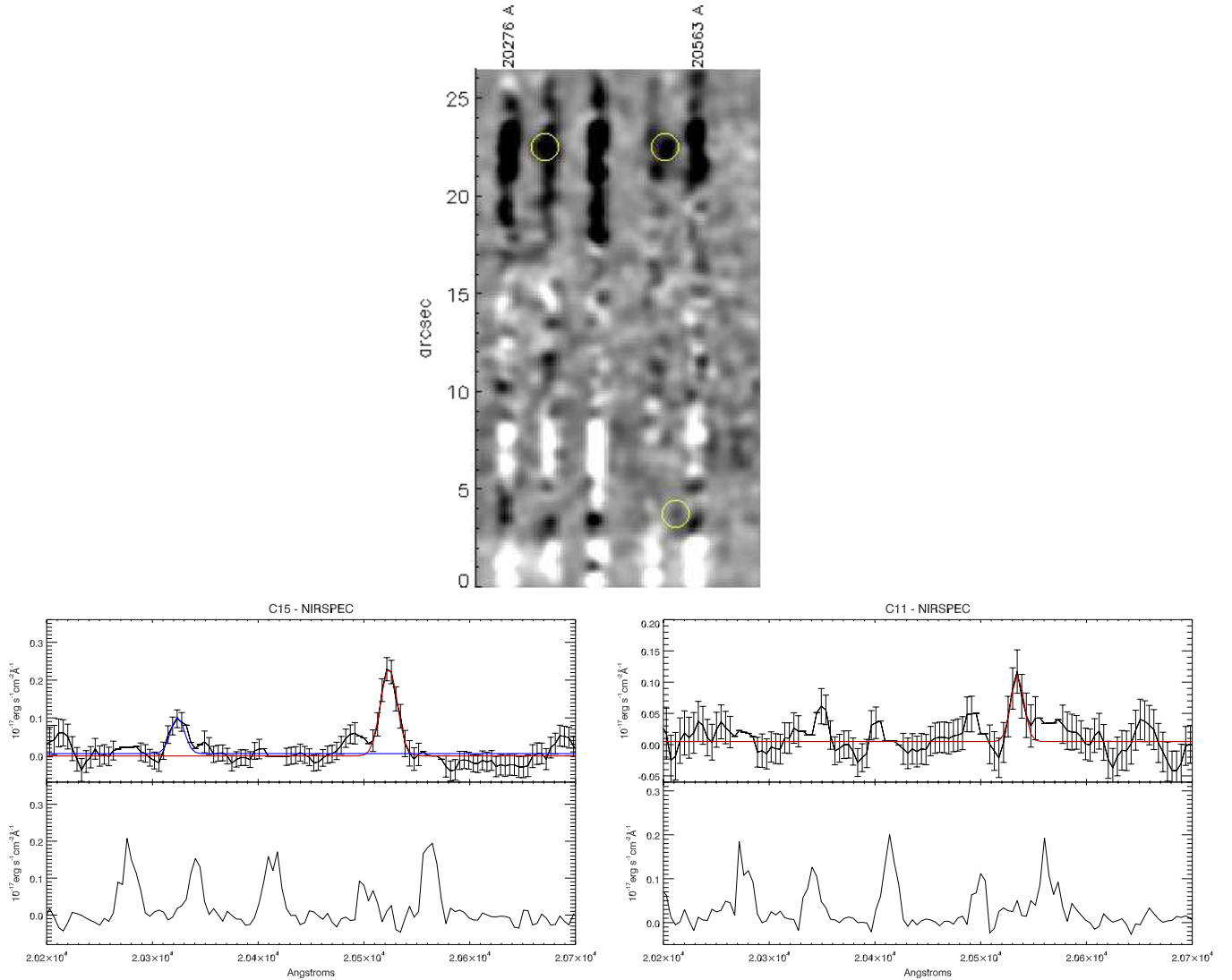
Figure 3. Top image is median combined, sky-subtracted, distortion corrected 2D spectrum from NIRSPEC. Top image has been smoothed with a Gaussian function with radius of three pixels. Emission lines from C11 and C15 are circled. [O III] doublet from C15 are upper circles, 5008.24 Å line from C11 is lower circle. Bottom row contains 1D NIRSPEC spectra for C15 and C11 (top panel) and extracted background. Best-fit Gaussians are overlaid on emission lines—see Section 5.1. Blue is 4960.295 Å line and red is 5008.24 Å line. Extracted background has been multiplied by −1 so one can easily recognize the sky lines, but the sky lines were actually negative in some places due to imperfect sky subtraction in the 2D image.

(A color version of this figure is available in the online journal.)

our NIRSPEC and LUCIFER slits. Next, we laid our LUCIFER and NIRSPEC slits (Figure 1) on the registered SAURON data and extracted the spaxels in the SAURON data that corresponded with the LUCIFER and NIRSPEC [O III] detections. This is essentially creating a virtual longslit aperture for the SAURON data. The LUCIFER longslit was 1″ wide and the NIRSPEC longslit was 0.″76 wide, so our virtual longslit for the SAURON data was 3 spaxels across, or 1.″2 to provide an approximate match to the LUCIFER and NIRSPEC apertures. The extracted spaxels were summed to create 1D spectra for C11 and C15. Because we observed C15 with both NIRSPEC and LUCIFER, with slightly different slit orientations, we extracted two spectra for C15—one that corresponds to our NIRSPEC slit orientation, and one that corresponds to our LUCIFER slit orientation. When discussing results for C15 below we specify whether the results are for C15 from the NIRSPEC alignment or C15 from the LUCIFER alignment. C11 was only detected with NIRSPEC, so we only extracted one spectrum for C11. The Lyα lines detected in the 1D spectra described above are shown in Figure 5.

To get error bars for the flux in the extracted 1D spectra we selected 1000 random spaxels in the SAURON datacube that were outside the area of the blob. At each wavelength we created a histogram of the 1000 flux values found in our random spaxels at that wavelength, fit a Gaussian to that histogram, and adopted the sigma of that Gaussian as the 1σ error on the flux at that wavelength.

5. RESULTS

5.1. [O III] Redshifts

As we did in McLinden et al. (2011) we fit detected [O III] lines with a single symmetric Gaussian plus a constant, using the IDL routine MPFITEXPR.[8] We fit the NIRSPEC and LUCIFER spectra independently. The central wavelength of the best-fit Gaussian determines the [O III] redshift. We fit the 4960.295 Å and 5008.24 Å lines independently for C15 in
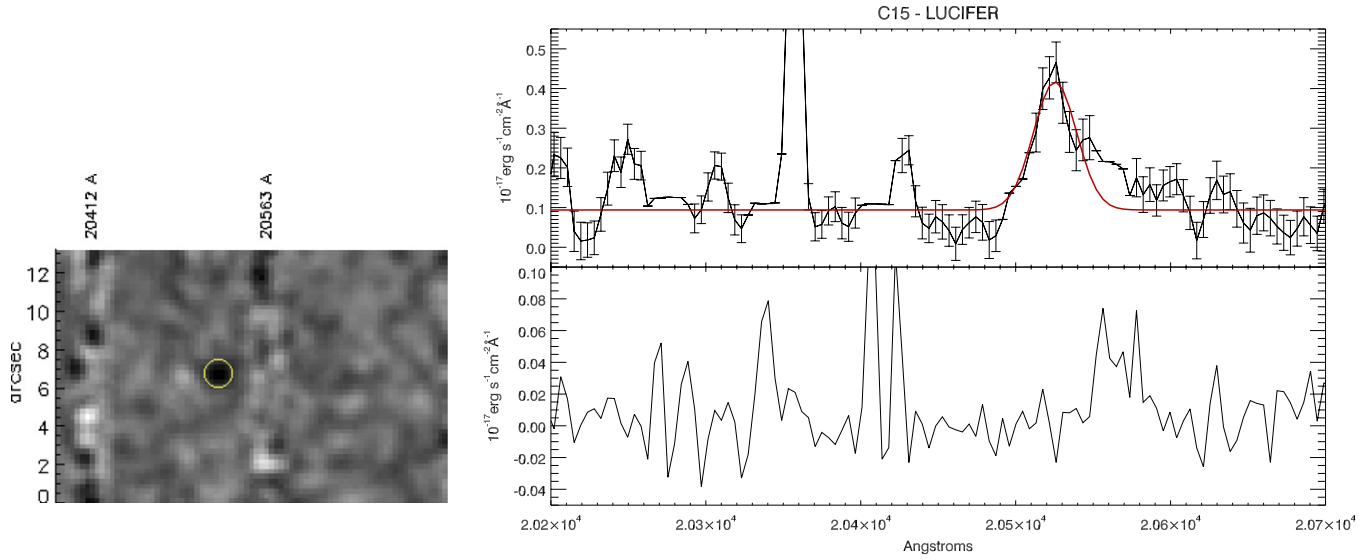
---

[8] http://cow.physics.wisc.edu/~craigm/idl/down/mpfitexpr.pro

Figure 4. Left plot is 2D LUCIFER spectrum of C15. The image has been smoothed by a Gaussian with a radius of 3 pixels and the [O III] detection (5008.24 Å) is circled. Right top panel is extracted 1D LUCIFER spectrum of C15. Feature at ∼20355 Å is a bad column. Best-fit Gaussian is overlaid on emission line—see Section 5.1. Bottom right panel is extracted background—only minimal sky line residuals remain because sky subtraction in 2D spectrum was excellent. Extracted background had been multiplied by −1.

(A color version of this figure is available in the online journal.)
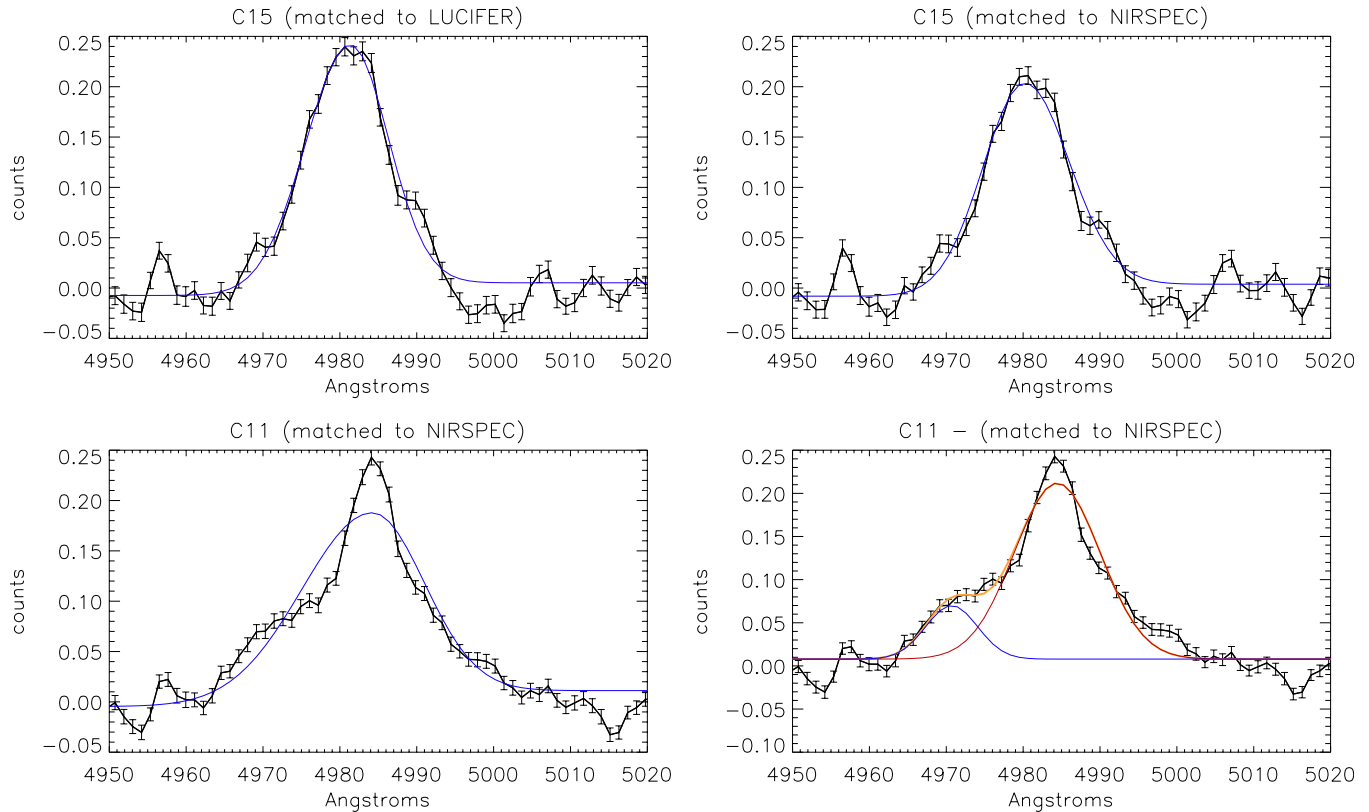
Figure 5. Best-fit Gaussians for C15 (top row) and C11 (bottom row) from ARM_ASYMGAUSSFIT show in blue. Lyα spectra are shown in black. Bottom right panel shows C11 simultaneously fit with a double Gaussian using MPFITEXPR—the two Gaussians are shown in blue and red, and their sum is shown in orange.

(A color version of this figure is available in the online journal.)

NIRSPEC and we find only the 5008.24 Å line in the LUCIFER data for this galaxy. Given the redshift of this region from the 5008.24 Å line in LUCIFER, the 4960.295 Å line should fall at ∼20332.3 Å, right on the edge of the 20339.497 Å (vacuum) OH emission line (Rousselot et al. 1999). This may explain why, after sky interpolation, we are unable to detect this line

in the slightly lower resolution of LUCIFER. The agreement between the redshift derived from 4960.295 and 5008.24 Å lines in NIRSPEC spectrum is good (see Table 1). We take the average of the 4960.295 Å and 5008.24 Å redshift as the derived systemic redshift for C15 from NIRSPEC, and use the redshift of the single line for C15 from LUCIFER.

<div align="center">

Table 1
Comparison of [O III] and Lyα Redshifts

</div>

Region	[O III]				Lyα	
	4960.295	5008.24	(z_{avg})	(z_{corr})	(z)	Δv (km s^{-1})
C15 (LUCIFER)		3.0983		**3.0986 ± 0.0003494**	**3.0976 ± 0.0004159**	−72.4 ± 41.6
C15 (NIRSPEC)	3.0973	3.0980	3.0976	**3.0974 ± 0.0005095**	**3.0967 ± 0.0002070**	−51.3 ± 42.1
C11 (NIRSPEC)		3.1002		**3.0999 ± 0.0003590**	**3.1000 ± 0.0002138**	5.8 ± 32.9

Notes. Comparison of [O III] and Lyα redshifts in C11 and C15 as measured with LUCIFER and NIRSPEC. z_{avg} is listed when the redshifts from 4960.295 and 5008.24 Å lines were averaged. z_{corr} is the redshift after correction to the LSR. Δv is velocity offset between [O III] and Lyα and is calculated by comparing the redshifts shown in bold.

Only the stronger 5008.24 Å line was detected in C11, and only in the NIRSPEC spectrum, so the 5008.24 Å line alone defined the redshift for this region. As mentioned in Section 3, the location of longslit in the LUCIFER setup was optimized for detection of R2 and C15, so it is not surprising that we did not have a detection for C11 in the LUCIFER data. All these [O III] redshifts were corrected for Earth's motion using topocentric radial velocities[9] appropriate for the date and location of the observations. The error bars on the redshift are a compilation of the rms from wavelength calibration during data reduction, the 1σ error on the best-fit central wavelength from Gaussian fitting, averaging of two redshifts when applicable, and a 0.02 km s^{-1} uncertainty on the topocentric radial velocities. See Table 1 for a summary of these data.

5.2. Lyα Redshifts

To determine the redshift of the Lyα emission line, we followed the same methodology we previously used in McLinden et al. (2011). Namely, the Lyα profiles for C11 and C15 were fit with a single asymmetric Gaussian plus constant, using IDL routine ARM_ASYMGAUSSFIT written by Andrew Marble. These fits are overlaid on the extracted 1D Lyα spectra in Figure 5. The asymmetric Gaussian fitting routine allows for, but does not require, the fit to be asymmetric. The central wavelength of the best-fit asymmetric Gaussian defines the Lyα redshift.

The error on the line center was determined from 1000 Monte Carlo iterations. In each iteration the flux at each wavelength was altered by a random amount proportional to the error bar at that point and the altered spectrum was re-fit with an asymmetric Gaussian. The standard deviation of the 1000 best-fit line centers is used as the 1σ error on the Lyα line center.

We note that the SAURON IFU datacube comes from a combination of data obtained in 2002 (Bower et al. 2004) and 2006 (Weijmans et al. 2010). The data were not corrected to the local standard of rest (LSR) before combination into a single datacube. Therefore, the Lyα profiles derived from the combined data may be slightly broadened with a slightly shifted center compared to the intrinsic Lyα profile. To account for this effect, we calculated the corrections that should be applied to the 2002 (~ -26.6 km s^{-1}) and the 2006 data ($\sim +2.1$ km s^{-1}).[10] Combining two such Gaussians, offset from one another by ~ 28.7 km s^{-1}, means that the intrinsic line center (if they had both been calibrated to the LSR before combination) is shifted by ~ 12.3 km s^{-1}. We therefore fold this 12.3 km s^{-1} term into our error calculations for redshift of the Lyα line and the subsequently derived [O III]–Lyα velocity offsets. Table 1 summarizes our Lyα and [O III] redshift information.

5.3. Velocity Offsets

We derive a velocity offset (Δv) between the [O III] and Lyα lines by comparing the redshifts for each line as derived from the central wavelength of the best-fit Gaussians to the two lines, where the fitting procedure is described above. We consider the [O III] redshift to be the systemic redshift. This method finds an offset between [O III] and Lyα in C15 of -72.4 ± 41.6 km s^{-1} from the LUCIFER data and -51.3 ± 42.1 km s^{-1} from the NIRSPEC data. These results are remarkably consistent with one another, despite being measured in slightly different apertures with different instruments. These results are modestly negative though also very nearly consistent with zero. We find Δv is 5.8 ± 32.9 km s^{-1} for C11 in the NIRSPEC data, which is consistent with no offset. Figure 6 illustrates these velocity offset measurements. Also see Table 1 for a compilation of these results.

One may argue that the rather broad Lyα line in C11 may be better fit with a double Gaussian profile, especially if one considers that the bump to the left of the highest peak is not noise, but in fact evidence of a second, unresolved peak. This could be a blue bump that is not fully resolved and separated from the main red peak. Or it could be the smaller red peak at $v = 0$, as in Figure 12 in Verhamme et al. (2006). To consider these possibilities, we fit C11 a second time, simultaneously fitting two Gaussians plus a constant (see the bottom right panel of Figure 5). When we do this we find that the right peak yields only a modest offset, where the Lyα line is offset by ~ 18 km s^{-1} from the [O III] redshift of C11 from NIRSPEC. The bluer Lyα peak is blueshifted with respect to [O III] by ~ 808 km s^{-1}. This leads to a rather inexplicably large offset between the two Lyα peaks, ~ 826 km s^{-1}, especially when the red peak is so mildly offset, which may disfavor this secondary interpretation of the modest bump as a blue bump. While acknowledgement of the additional fit described above is worthwhile, the discussion stays much the same, the observed velocity offset between [O III] (systemic) and Lyα is at best modestly negative and/or may be consistent with zero.

5.4. [O III] Flux in C15 and R2

As previously described in Section 5.1, the [O III] lines are fit with a symmetric Gaussian plus a constant. The resulting area under the Gaussian gives us a line flux measurement for each line. We find an [O III] flux of $1.1 \pm 0.1 \times 10^{-16}$ erg s^{-1} cm^{-2} for C15 from LUCIFER (5008 Å line only). For C15 in NIRSPEC we find line fluxes of $1.6 \pm 0.5 \times 10^{-17}$ erg s^{-1} cm^{-2} (4960 Å) and $4.6 \pm 0.5 \times 10^{-17}$ erg s^{-1} cm^{-2} (5008 Å). Finally, for C11 from NIRSPEC we measure a line flux of $1.6 \pm 0.4 \times 10^{-17}$ erg s^{-1} cm^{-2} (5008 Å line only).

Since we do not detect an [O III] line in R2 we instead measure an [O III] line flux upper limit of $\leqslant 3.4 \times 10^{-17}$ erg s^{-1} cm^{-2}.
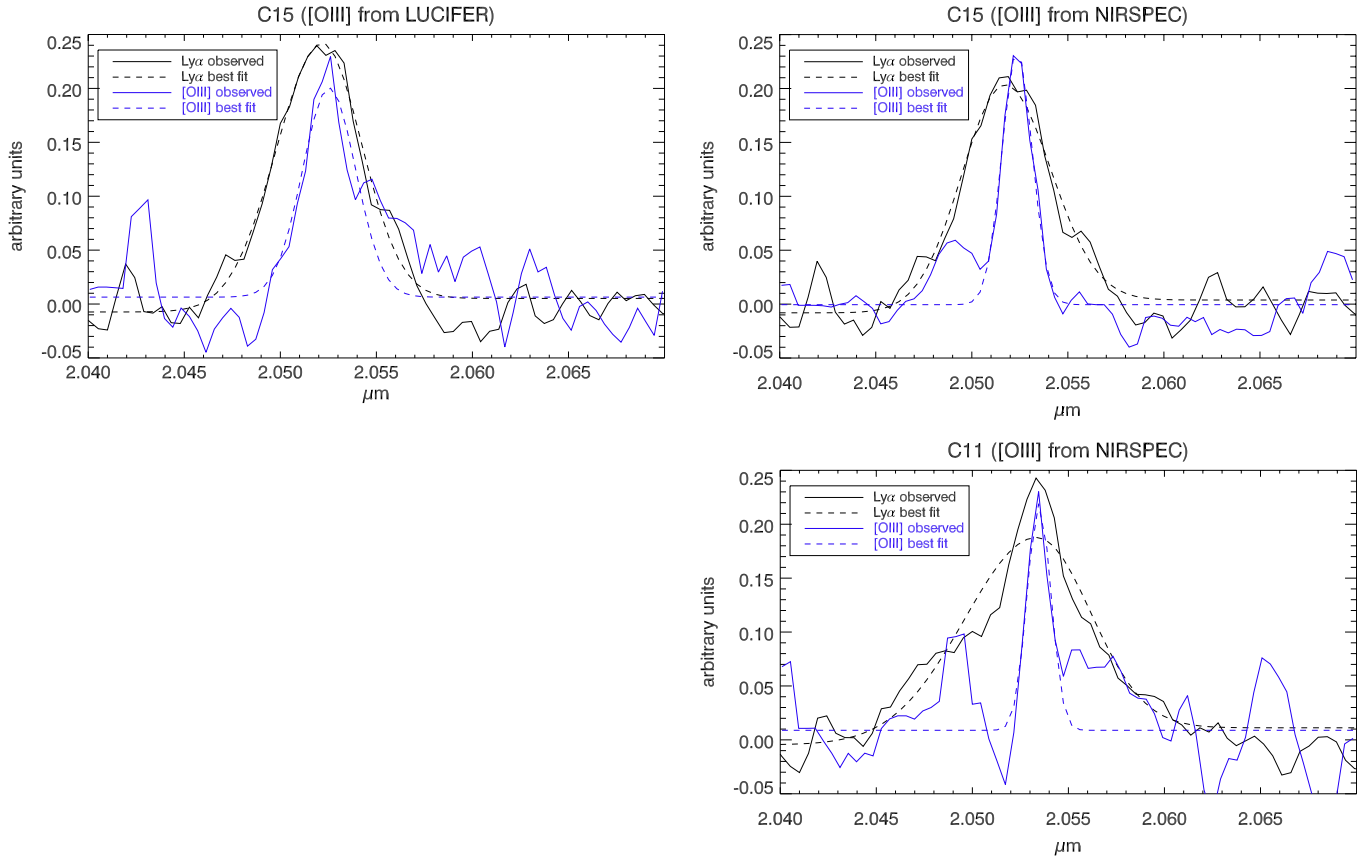
Figure 6. Plot of Lyα (blue) over [O III] (black) where Lyα has been shifted to [O III] frame via $\mathrm{Ly}\alpha_{[O\,III]} = \mathrm{Ly}\alpha_{observed} \times (5008.24/1215.67)$. Observed spectra are shown with solid lines, best-fit Gaussians for both Lyα and [O III] are shown with dashed lines. Top panel is C15, the left plot shows [O III] from LUCIFER, and the right plot shows [O III] from NIRSPEC. Bottom panel is C11 from NIRSPEC.

(A color version of this figure is available in the online journal.)

LUCIFER has sufficient wavelength coverage to place upper limits on both [O II] and Hβ in our C15 spectrum. We derive upper limits for [O II] and Hβ in C15 of 1.3×10^{-17} and 2.2×10^{-16} erg s^{-1} cm^{-2} from our LUCIFER spectrum. This combination of a measured [O III] line flux and upper limits on [O II], and Hβ line flux in C15 allow us to put constraints on the metallicity of the LBG embedded in C15 using R_{23}, where R_{23} is defined as ([O II] + [O III]/Hβ) (Pagel et al. 1979; Kewley & Dopita 2002). For C15, $R_{23} > 0.76$ given the line flux measurements and limits described above. NIRSPEC wavelength coverage only allows us to place upper limits on Hβ. We find Hβ upper limits of 3.7 and 7.2×10^{-18} erg s^{-1} cm^{-2} for C15 and C11, respectively.

To compute the 3σ line flux upper limit for R2 quoted above, we added a mock Gaussian emission line to the spectra to represent [O III], similar to the procedure in Finkelstein et al. (2011). The sigma of the Gaussian was fixed to 5.52 Å, or the σ from our faintest [O III] detection to date (McLinden et al. 2011). The area under the mock line was measured using a symmetric Gaussian, this area determines the line flux of the mock line. Then we determined the noise on the line flux measurement from 1000 Monte Carlo iterations, where the flux array was modified each time by a random amount proportional to the error bars. We repeated this process, each time decreasing the area under the mock Gaussian until the signal-to-noise ratio (S/N) dropped below 5σ. The line flux in the mock line where the S/N crossed below 5σ determines σ. However, because one cannot know without an nebular emission line measurement

for reference exactly how much, if any, the Lyα line is offset from the [O III] line, we repeat this calculation, fixing the mock line at different redshifts to mimic different velocity offsets. We found the 3σ [O III] line flux detection limit as an average of this technique from six different redshifts corresponding to velocity offsets of 0–500 km s^{-1}, in increments of 100 km s^{-1}. A range of 0–500 km s^{-1} was chosen to mirror the magnitude of Lyα -[O III] velocity offsets we have observed of 52–342 km s^{-1} in three $z \sim 3.1$ LAEs. The range of 3σ detection limits over this wavelength range was 3.12–3.54×10^{-17} erg s^{-1} cm^{-2}. The [O II] and Hβ upper limits described above are found using the same procedure, except the upper limits need only be derived at a single fixed wavelength for each line, the wavelength defined by the [O III] redshift.

Given [O III] line flux detections in C15 and C11 and an [O III] upper limit in R2, we can compare the nebular emission from these subregions. This is of interest because C15 and C11 are associated with LBGs embedded within the larger LAB1 halo structure, whereas R2, in spite of its stronger Lyα emission, is not associated with any underlying galaxy (Weijmans et al. 2010). The ratio of Lyα luminosity in C15 to R2 is 0.7 (Weijmans et al. 2010). We find that the ratio of [O III] in C15 (LUCIFER) to R2 is $\geqslant 3.4$ and the ratio of [O III] in C15 (NIRSPEC) to R2 is $\geqslant 1.4$, meaning that while R2 is brighter in Lyα C15 is brighter when looking at [O III] nebular emission. Finally, the [O III] to Lyα ratio measured in the region without an LBG is therefore at least 1.9–4.5 times smaller than the same ratio measured in the LBG. This measurement would likely indicate that something

other than star formation is powering the Lyα emission in region R2 and that there may very well be different sources powering Lyα emission in different regions of the same blob.

C11 presents a somewhat different story. The ratio of Lyα luminosity in C11 to R2 is 1.0 (Weijmans et al. 2010). Then the ratio of [O III] in C11 (from NIRSPEC) to R2 is only $\geqslant 0.5$. The [O III] to Lyα in C11 is only 0.06, which is smaller than that same measurement in R2, where the ratio is $\leqslant 0.13$. These divergent results are interesting, perhaps giving further credence to the idea that there are different processes at work in different regions of this blob.

5.5. Asymmetry and [O III]–Lyα Offset

We have now measured the velocity offset between [O III] and Lyα in 3 $z \sim 3.1$ LAEs (McLinden et al. 2011) and added three Δv measurements for LAB1 in this work. Among these measurements, the regions C11 and C15 in LAB1 have the smallest absolute Δv measurements and are the only negative values. This is in contrast to three $z \sim 3.1$ LAEs in which we found offsets ranging from 52 to 342 km s^{-1}. Given this information, we can compare another signature of outflows, namely asymmetry in the Lyα profile, with the velocity offset measurements.

We quantify asymmetry as $\sigma_{\rm red}/\sigma_{\rm blue}$ where $\sigma_{\rm red}$ is the sigma of the red side of the best-fit asymmetric Gaussian and $\sigma_{\rm blue}$ is the sigma on the blue side of the best-fit asymmetric Gaussian, where both are parameters returned by the ARM_ASYMGAUSSFIT routine. With this definition, a profile with asymmetry >1.0 is considered asymmetric, and the asymmetry is dominated by the red-wing. Objects with asymmetry = 1.0 are symmetric, $\leqslant 1.0$ have blue-wing dominated asymmetry. The red-wing-dominated asymmetry is the expected direction of the asymmetry in the Lyα line from high-z galaxies, as the red side of the line can be enhanced in the presence of an expanding shell (Verhamme et al. 2006; Dijkstra & Wyithe 2010) and/or by interaction with neutral hydrogen in the intergalactic medium (Rhoads et al. 2003; Dawson et al. 2004). Measured in this way C11 has an asymmetry of 0.74 ± 0.02 and C15 has an asymmetry of 0.9 ± 0.03 and 1.1 ± 0.03 (LUCIFER and NIRSPEC apertures, respectively). An asymmetry of <1.0, like C11, can suggest infalling material. However, the Lyα-[O III] velocity offset of 5.8 ± 32.9 km s^{-1} in C11 is not very supportive of such an interpretation. In three $z \sim 3.1$ LAEs in which we have measured a velocity offset between [O III] and Lyα we find asymmetries of 0.97 ± 0.1, 1.04 ± 0.1, and 1.65 ± 0.1 for LAE7745, LAE27878, and LAE40844, respectively (McLinden et al. 2011). We add four additional asymmetry data points by using four $z \sim 2$ LAEs from Hashimoto et al. (2013). Hashimoto et al. (2013) measured redshifted Lyα lines in these objects with respect to Hα lines in the same objects. They report velocity offsets of 18–190 km s^{-1} in their four LAEs, in good agreement with our range of 52–342 km s^{-1} in LAEs. We measured the asymmetry of the Lyα lines presented by Hashimoto et al. (2013) in the same manner as above, by fitting each line with asymmetric Gaussian and quantifying asymmetry as $\sigma_{\rm red}/\sigma_{\rm blue}$. Measured in this way the LAEs from Hashimoto et al. (2013) have asymmetries of 0.53–1.7.

Figure 7 demonstrates a possible trend where asymmetry in the Lyα profile increases with increasing velocity offset. We find a moderate Pearson linear correlation coefficient of 0.427 ($P = 0.110$) between the velocity and asymmetry values, suggesting the trend may be real. This velocity–asymmetry correlation is not unexpected, as increasing (red-wing-dominated) asymmetry
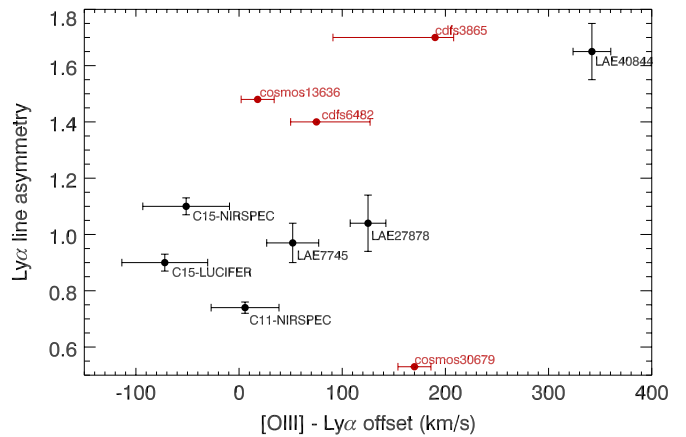

Figure 7. Asymmetry of the Lyα profile as a function of velocity offset in five Lyα-emitting objects at $z \sim 3.1$ (shown in black) and four $z \sim 2$ objects (shown in red). Three LAEs from McLinden et al. (2011) are labeled with the prefix "LAE." Red points with the prefix "cosmos" or "cdfs"zz are from Hashimoto et al. (2013). Overall, asymmetry may increase with increasing velocity offset. (A color version of this figure is available in the online journal.)

in the Lyα profile is tied to increasing shell expansion velocities in Verhamme et al. (2006), when outflows are modeled with a central monochromatic source and an expanding shell. This is because Lyα photons are seen as more redshifted by the neutral hydrogen in the shell with higher shell expansion speeds, decreasing the cross-section for interaction (Verhamme et al. 2006). A symmetric line, as seen in C15, is not expected in models with large outflows, but could be consistent with static/nearly static profiles—if the two symmetric peaks produced from a static slab or shell scenario (Verhamme et al. 2006) are unresolved. The authors note that the point attributed to LAE40844 strongly influences this correlation. Removal of this point and recalculation of the Pearson coefficient with the remaining eight points only yields a coefficient of 0.170 ($P = 0.331$), which does not suggest any significant correlation.

6. DISCUSSION

6.1. Comparison with Blobs at $z \sim 2$

We have measured Δv between [O III] and Lyα in two subregions of LAB1 and found that Δv is modestly negative or consistent with 0 km s^{-1}. These measurements seem to downplay the role of powerful outflows in powering the Lyα in these regions and could even hint at some infall. Interestingly, this measurement of $\Delta v =$ small is not the first time this phenomenon has been reported in a Lyα blob, suggesting this is an important phenomenon that must be explored to better understand the nature of high-z LABs. Yang et al. (2011) investigated two $z \sim 2.3$ LABs, where one blob (called CDFS-LAB02) had $\Delta v \sim 230$ km s^{-1} and the other blob had Δv consistent with zero (called CDFS-LAB01). The velocity offsets reported in Yang et al. (2011) were measured by comparing the redshift of Hα to that of Lyα, a very similar tactic to our comparison of [O III] to Lyα, as both [O III] and Hα are nebular emission lines and therefore probe the same regions.

6.2. Comparison to LAEs and LBGs

Our Δv measurements, and those of Yang et al. (2011), are significantly less than the larger velocity offsets typically seen in LBGs and even LAEs, velocity offsets which are typically interpreted as clear signatures of strong winds in these galaxies.

Steidel et al. (2010) report median velocity offsets between Hα and Lyα of 445 km s^{-1} in 41 $z \sim 2.3$ LBGs. Even LAEs, whose typical velocity offsets have been found to be smaller, have Δv as large as 342 km s^{-1} (McLinden et al. 2011).

Steidel et al. (2010) also report a median velocity offset between Hα and strong interstellar absorption lines of -164 km s^{-1} in 86 LBGs, which further supports interpretations of the presence of outflows in LBGs, since the blueshifted absorption implies absorption in material moving toward the observer. Shapley et al. (2006) previously measured a redshift from low-ionization interstellar absorption (LIS) lines in the LBG C11, finding that the absorption lines are offset from the Lyα line by -380 km s^{-1}. Using the LIS redshift of 3.0962 from Shapley et al. (2006) and comparing this to the Lyα redshift we derive for C11 yields an offset of ~ 278 km s^{-1}. Comparing our [O III] (systemic) redshift for C11 (3.0999) to the LIS redshift, we can estimate that the LIS lines in C11 are offset from [O III] by ~ -270 km s^{-1}. This comparison of Lyα and [O III] redshifts to LIS absorption redshifts provides a stronger signature of an outflow than we get when comparing Lyα and [O III]. In fact, it is particularly interesting that the magnitude of this second signature of winds (i.e., blueshifted interstellar absorption lines) is so similar when comparing the Steidel LBGs to C11, yet the magnitude of the offset between nebular emission lines (Hα or [O III]) and Lyα offset are so different. We note that the lack of Δv between [O III] and Lyα does not have to rule out some outflows in LAB1. Rather, the lack of a Lyα-[O III] offset may just imply that outflows are not a significant mechanism for helping Lyα photons escape.

6.3. Previous Studies of LAB1

This phenomenon, i.e., Δv = small and/or = 0 km s^{-1}, leads to the question of whether the lack of substantial velocity offset between Hα–Lyα or [O III]–Lyα in these blobs in fact rules out outflows or if there is some yet to be understood phenomena that damps or erases this particular wind signature. This question is particularly relevant given the recent report from Hayes et al. (2011) that there is polarized radiation emanating from LAB1, polarization that is indicative of scattering of Lyα photons at large radii with respect to their site of production. This may be a sign of outflows helping to drive the Lyα photons to these large radii, but we are not seeing the velocity offsets between nebular emission lines and Lyα that we would expect to see if this was the case, velocity offsets we have been able to see in other objects at similar redshifts believed to have strong winds. In addition, Bower et al. (2004) and Weijmans et al. (2010) both measure a velocity shear in the Lyα emission from C11 and C15. As the authors point out, such a velocity shear could be consistent with infalling gas, outflowing gas, and/or rotation of the system, and such scenarios cannot be differentiated from the Lyα data alone. While both papers use this velocity shear to argue in favor of the presence of outflows in C11 and C15, we can report no signature of such outflows when we compare the redshifts of [O III] and Lyα, a comparison that has proven to be a useful diagnostic of winds in LAEs and LBGs at similar redshifts.

6.4. Comparison to Radiative Transfer Models

We explored available Lyα radiative transfer models to see if there were any models that might shed light on the physical conditions that could lead to a modestly negative Δv or Δv of ~ 0 km s^{-1} between [O III] (or Hα) and Lyα. We focused on the

Lyα profiles produced by Verhamme et al. (2006, henceforth V06) from their 3D Monte Carlo Lyα radiative transfer code. V06 explore a variety of physical conditions and geometric orientations to explore the diversity of Lyα profiles that arise from different conditions. See V06 for extensive details on these models and the model parameters. We find, however, that none of the models presented in V06 are in great agreement with our observations (or the observations of Yang et al. 2011). The only models that are marginally consistent with our observations are those that have two significant Lyα peaks, where the centroid of those two peaks is centered at $v \sim 0$, with one peak redward of $v = 0$, and the other blueward. Convolved with an appropriate Gaussian to mimic the instrumental resolution of SAURON (290 km s^{-1}), these models somewhat resemble the Lyα profiles presented here. This double-peaked, centered at $v \sim 0$ profile occurs when a central monochromatic source is embedded in a static slab (with or without dust; V06 Figure 3), a central monochromatic source sits in a non-expanding shell (V06 Figure 14), and when a single monochromatic source sits in an expanding shell with very small velocity gradient (V max $= 20$ km s^{-1}; V06 Figure 7). The closest match (see Figure 8) is from V06, Figure 14 with a static shell. In addition, we explored whether the infalling halo models of V06 might agree with our observations, these models are presented in Figure 9. There may be some qualitative agreement between the models and observed profiles here, but the models explored are too far blueward of $v = 0$ to match the Lyα profiles we present here. In either scenario (expanding or infalling) the main peak is expected to be asymmetric, which is inconsistent with the Lyα profiles of at least C15 presented here. We contend that more modeling of Lyα radiative transfer with direct applications to the observations we have presented here and those observations presented in Yang et al. (2011) needs to be done, to better understand the physical conditions, geometry, and kinematics that can produce single-peaked Lyα lines, with Δv values that are modestly negative or consistent with zero.

7. CONCLUSION

We have measured [O III] in two subregions of LAB1, C11, and C15, regions that are associated with underlying LBGs within the larger halo structure. We have quantified the velocity offset between [O III] and Lyα redshifts in these regions, finding that both measurements are modestly negative or consistent with zero. This is an intriguing result since powerful outflows have been proposed as possible ways to explain the luminosity and large spatial extent of LABs. We cannot completely rule out the presence of strong winds and outflows in LAB1, but we can state that we do not see two typical markers of their presence. (1) The aforementioned result that we do not find that Lyα is redshifted with respect to [O III] in the two LAB1 subregions C15 and C11. (2) We do not measure strong red-wing-dominated asymmetries in the Lyα profiles of these objects, in contrast with $z \sim 2$ and $z \sim 3.1$ LAEs where the asymmetry of the Lyα line appears to increase with increasing velocity offset between [O III] (or Hα) and Lyα. If outflows are present in LAB1, they do not appear to be a crucial mechanism driving Lyα escape.

In addition to the conclusion above, we have placed an upper limit on [O III] line flux from region R2, a subregion of LAB1 unassociated with any known galaxy and compared this to the [O III] flux from subregion C15, which is associated with an LBG. We find that in spite of the strong Lyα emission present in R2, the [O III] flux from C15 is stronger than that of R2 by at least 1.4–2.5 times. This measurement may indicate that diverse
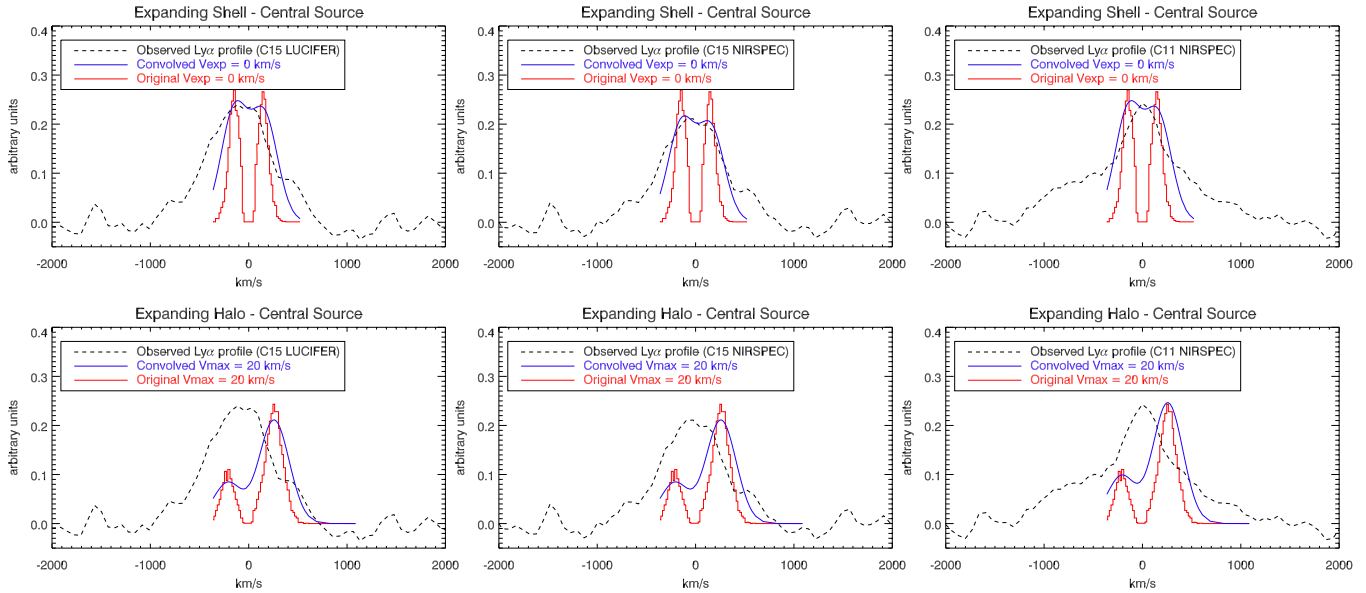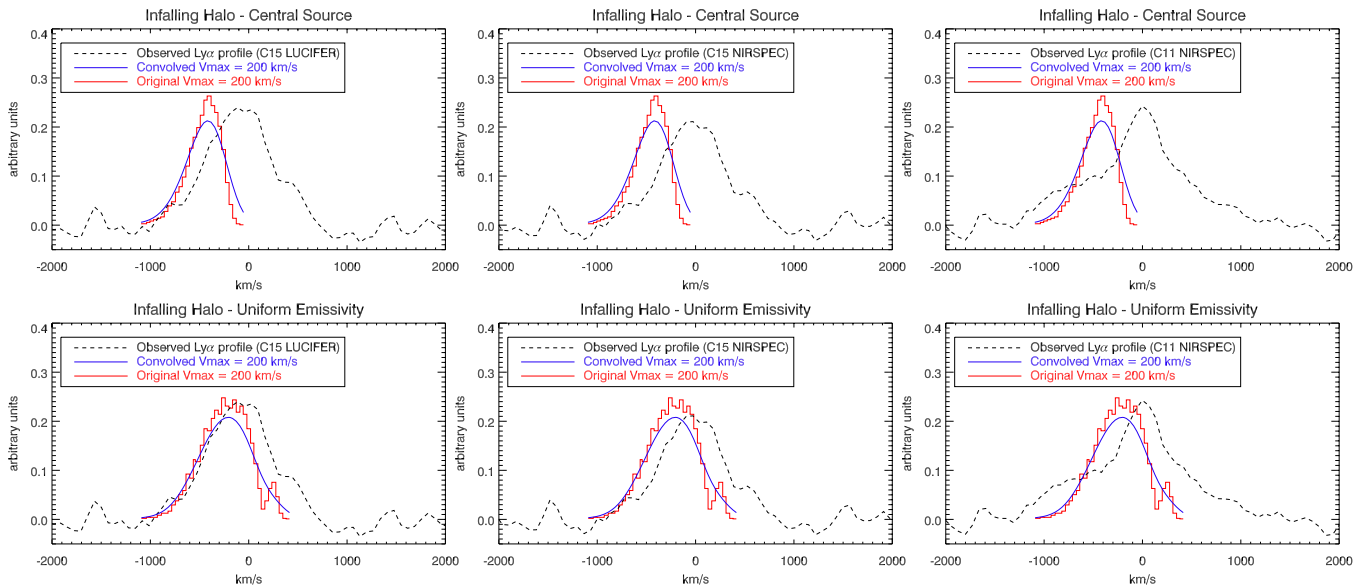
Figure 8. Lyα profiles (black dashed line) compared to V06 outflowing shell and halo models. Original V06 models (red) have been convolved with a Gaussian to match instrumental resolution of SAURON (blue). Top row shows comparison to model in V06 Figure 14. Bottom row shows comparison to model in V06 Figure 7. While these models and those in Figure 9 represent the closest matches to the observed profiles, clearly none are an excellent fit.

(A color version of this figure is available in the online journal.)

Figure 9. Lyα profiles (black dashed line) compared to V06 infalling halo models. Original V06 models (red) have been convolved with a Gaussian to match instrumental resolution of SAURON (blue). Top row shows comparison to model in left panel of Figure 5 in V06 and the bottom row shows comparison to model in the right panel of Figure 5. While these models and those in Figure 8 represent the closest matches to the observed profiles, clearly none are an excellent fit.

(A color version of this figure is available in the online journal.)

sources of Lyα emission may be responsible for powering different regions even within the same blob.

REFERENCES

Ageorges, N., Seifert, W., Jütte, M., et al. 2010, Proc. SPIE, 7735, 53A
Bacon, R., Copin, Y., Monnet, G., et al. 2001, MNRAS, 326, 23
Bower, R. G., Morris, S. L., Bacon, R., et al. 2004, MNRAS, 351, 63
Chapman, S. C., Lewis, G. F., Scott, D., et al. 2001, ApJL, 548, L17
Chapman, S. C., Scott, D., Windhorst, R. A., et al. 2004, ApJ, 606, 85
Chapman, S. C., Windhorst, R., Odewahn, S., et al. 2003, ApJ, 599, 92
Cowie, L. L., & Hu, E. M. 1998, AJ, 115, 1319
Dawson, S., Rhoads, J. E., Malhotra, S., et al. 2004, ApJ, 617, 707
Dey, A., Bian, C., Soifer, B. T., et al. 2005, ApJ, 629, 654
Dijkstra, M., & Loeb, A. 2009, MNRAS, 400, 110
Dijkstra, M., & Wyithe, J. S. B. 2010, MNRAS, 408, 352
Finkelstein, S. L., Cohen, S. H., Moustakas, J., et al. 2011, ApJ, 733, 117
Francis, P. J., Williger, G. M., Collins, N. R., et al. 2001, ApJ, 554, 1001
Geach, J. E., Alexander, D. M., Lehmer, B. D., et al. 2009, ApJ, 700, 1
Geach, J. E., Smail, I., Chapman, S. C., et al. 2007, ApJL, 655, L9
Haiman, Z., Spaans, M., & Quataert, E. 2000, ApJ, 537, 5
Hashimoto, T., Ouchi, M., Shimasaku, K., et al. 2013, ApJ, 765, 70
Hayes, M., Scarlata, C., & Siana, B. 2011, Natur, 476, 304
Hu, E. M., Cowie, L. L., & McMahon, R. G. 1998, ApJL, 502, L99
Kelson, D. 2003, PASP, 115, 688
Kewley, L. J., & Dopita, M. A. 2002, ApJS, 142, 35
Kohno, K., Tamura, Y., Hatsukade, B., et al. 2008, in ASP Conf. Ser. 399, Panoramic Views of Galaxy Formation and Evolution, ed. T. Kodama, T. Yamada, & K. Aoki (San Francisco, CA: ASP), 264
Matsuda, Y., Yamada, T., Hayashino, T., et al. 2004, AJ, 128, 569
McLean, I. S., Becklin, E. E., Bendiksen, O., et al. 1998, Proc. SPIE, 3354, 566
McLinden, E., Finkelstein, S., Rhoads, J., et al. 2011, ApJ, 730, 136
Nilsson, K. K., Fynbo, J. P. U., Møller, P., Sommer-Larsen, J., & Ledoux, C. 2006, A&A, 452, L23
Ohyama, Y., Taniguchi, Y., Kawabat, K. S., et al. 2003, ApJ, 591, 9
Pagel, B. E. J., Edmunds, M. G., Blackwell, D. E., et al. 1979, MNRAS, 189, 95
Pickles, A. J. 1998, PASP, 110, 863
Prescott, M. K., Dey, A., & Jannuzi, B. T. 2012, ApJ, 748, 125
Prescott, M. K., Smith, P. S., Schmidt, G. D., & Dey, A. 2011, ApJ, 730, 25
Rhoads, J. E., Dey, A., Malhotra, S., et al. 2003, AJ, 125, 1006
Rhoads, J. E., Malhotra, S., Dey, A., et al. 2000, ApJL, 545, L85
Rousselot, P., Lidman, C., Cuby, J.-G., et al. 2000, A&A, 354, 1134
Seifert, W., Appenzeller, I., Baumeister, H., et al. 2003, Proc. SPIE, 4841, 962
Shapley, A. E., Steidel, C. C., Pettini, M., et al. 2006, ApJ, 651, 688
Spergel, D. N., Bean, R., Doré, O., et al. 2007, ApJS, 170, 377
Steidel, C. C., Adelberger, K. L., Dickinson, M., et al. 1998, ApJ, 492, 428
Steidel, C. C., Adelberger, K. L., Shapley, A. E., et al. 2000, ApJ, 532, 170
Steidel, C. C., Erb, D. K., Shapley, A. E., et al. 2010, ApJ, 717, 289
Taniguchi, Y., & Shioya, Y. 2000, ApJ, 532, 13
Verhamme, A., Schaerer, D., & Maselli, A. 2006, A&A, 460, 397
Weijmans, A.-M., Bower, R. G., Geach, J. E., et al. 2010, MNRAS, 402, 2245
Yang, Y., Decarli, R., Dannerbaurer, H., et al. 2012, ApJ, 744, 178
Yang, Y., Zabludoff, A., Jahnke, K., et al. 2011, ApJ, 735, 87